

**Probable detection of starlight reflected from the giant exoplanet  
orbiting  $\tau$  Boötis**

*By Andrew Collier Cameron\*, Keith Horne\*, Alan Penny<sup>†</sup> and David James\**

*\* School of Physics and Astronomy, University of St Andrews,  
North Haugh, St Andrews, Fife KY16 9SS*

*<sup>†</sup> Rutherford Appleton Laboratory, Chilton, Didcot, Oxon OX11 0QX*

**THIS RESULT IS UNDER STRICT EMBARGO  
TO NATURE**

Giant planets orbiting stars other than the Sun are clearly detectable through precise radial-velocity measurements of the orbital reflex motion of the parent star. In the four years since the discovery<sup>1</sup> of the companion to the star 51 Peg, similar low-amplitude “Doppler star wobbles” have revealed the presence of some 20 planets orbiting nearby solar-type stars. Several of these newly-discovered planets<sup>2, 3, 4</sup> are very close to their parent stars, in orbits with periods of only a few days. Being an indirect technique, however, the reflex-velocity method has little to say about the sizes or compositions of the planets, and can only place lower limits on their masses. Here we report the use of high-resolution optical spectroscopy to achieve a probable detection of the

Doppler-shifted signature of starlight reflected from one of these objects, the giant exoplanet orbiting the star  $\tau$  Boötis. Our data give the planet's orbital inclination  $i = 29^\circ$ , indicating that its mass is some 8 times that of Jupiter, and suggest strongly that the planet has the size and reflectivity expected for a gas-giant planet.

A planet orbiting a star scatters back into space some of the starlight it receives. To a distant observer, the ratio of the scattered flux  $f_p$  from the planet to the direct flux  $f_\star$  from its star depends on the planet's size and proximity to the star, which determine the amount of light intercepted, and on the scattering properties of the planet's atmosphere. For a planet of radius  $R_p$  in an orbit of radius  $a$ , the planet-to-star brightness ratio is  $\epsilon \equiv f_p/f_\star = p(\lambda, \alpha)(R_p/a)^2$ , where  $p(\lambda, \alpha)$  is the geometric albedo of the atmosphere for light of wavelength  $\lambda$  when viewed at an angle  $\alpha$  relative to the sub-stellar point. The  $\tau$  Boo planet<sup>2</sup> has a circular orbit with a radius  $a = 0.0462(M_\star/1.2 M_\odot)^{1/3}$  AU, derived from Kepler's law with the 3.3 d orbital period and estimated stellar mass. If this is a giant planet, with a Jupiter-like size and albedo, we expect  $\epsilon \sim 10^{-4}$ ; the scattered starlight will be 10,000 to 20,000 times fainter than the star even when viewed at the most favourable illumination angle  $\alpha = 0$ .

Although  $\tau$  Boo and its planet are never separated on the sky by more than 0.003 seconds of arc, this close-in planet orbits its star with a relatively large velocity  $V_p = 152 \text{ km s}^{-1}$ , based on observations of the star's reflex motion<sup>2</sup>. The star and planet may therefore be easier to separate by using the orbital Doppler shift than by direct imaging. The pattern of photospheric absorption lines in the starlight is preserved when the starlight is reflected from the planet, apart from the Doppler shift due to the planet's orbital velocity, and a multiplicative scaling by the wavelength-dependent albedo of its atmosphere. If the planet's orbit is inclined by an angle  $i$

relative to our line of sight, its Doppler shift varies between  $-K_p$  and  $+K_p$  as it orbits around the star, where  $K_p = V_p \sin i$ . For comparison, the star’s absorption lines span  $\pm 28 \text{ km s}^{-1}$ , largely due to the star’s rotation. Except in the unlikely case of a nearly face-on orbit,  $i < 10^\circ$ , the orbital Doppler shift should cleanly separate the planet’s spectral lines from those of the star.

We observed  $\tau$  Boo for a total of 48 hours on four nights in 1998 April and five further nights in 1999 April, May and June using the Utrecht Echelle Spectrograph on the 4.2-m William Herschel Telescope at the Roque de los Muchachos Observatory on La Palma. The ranges in orbital phase covered by each night’s observations are listed in Table I.

To isolate the feeble scattered-light spectrum of  $\tau$  Boo’s planet, we begin by constructing a high fidelity spectral model to accurately subtract the direct starlight from each of the 580 spectra. The initial stellar spectrum subtraction is a delicate operation. Small shifts of the spectrum on the detector and changes in the telescope focus and atmospheric seeing distort the spectral-line profiles from each exposure to the next. Even small distortions of the strong stellar lines can produce changes larger than the faint signature of the planet. We therefore calibrate these instrumental distortions by comparing each spectrum with a “template” spectrum  $T(\lambda)$ , which we construct by adding together all other spectra secured on the same night. Making a new template for each night, rather than a single template for the whole observing run, helps to remove small changes in the detector response pattern from one night to the next. The stability of the spectrograph is such that all spectra secured on a given night are mutually aligned to within 0.2 pixel ( $0.6 \text{ km s}^{-1}$ ), so that the template spectra are not appreciably broadened. Our template spectra have a signal-to-noise ratio exceeding  $10^4$  per spectral pixel in the best-exposed parts of the image.

We model each of the individually distorted stellar spectra as a linear combination of the template and its first and second derivatives with respect to wavelength

$$S(\lambda, \phi) = a_0 T(\lambda) + a_1 \frac{\partial T(\lambda)}{\partial \lambda} + a_2 \frac{\partial^2 T(\lambda)}{\partial \lambda^2} .$$

The line spread function (LSF) in our spectra is only 2.1 pixels wide (6.4 km/s), but the star’s rotation spreads the stellar line profiles across 18 pixels (55 km s<sup>-1</sup>). The above approximation is therefore adequate (in terms of stability against “ringing” and other related sampling effects) to correct the 0.2-pixel shifts and  $\sim 0.5$ -pixel seeing-induced changes we see in width of the LSF. The coefficient  $a_0$  serves to scale the template to match the observed spectrum,  $a_1$  models the pixel shift between the spectrum and the template, and  $a_2$  accounts for small changes in the width of the LSF due primarily to changes in atmospheric seeing. We at first included higher derivatives to model changes in the skew and kurtosis of the LSF, but concluded that these effects were not significant. To account for small changes in the LSF of the spectrograph across the focal plane, we represent the three coefficients as spline functions that vary smoothly across the frame. We optimize the spline functions to fit each spectrum, using an iterative least-squares fit with outlier rejection, and then subtract the optimized model from each observed spectrum in turn.

This procedure very effectively removes the direct starlight signal, leaving the planet signal deeply buried in noise. The procedure of constructing a template spectrum to model the direct starlight spectrum inevitably incorporates into the template some part of the planet signal. This is particularly troublesome near the quadrature phases 0.25 and 0.75, when the planet’s velocity is approximately constant. Subtracting the template thus modifies and eliminates some of the planet signal. We account for this partial suppression later in the signal extraction process.

After subtracting the template to remove the stellar spectrum, we add together groups of four contiguous observations, primarily to save computer time in the subsequent analysis. This reduces the number of spectra from 580 to 145, and boosts the signal-to-noise ratio to  $\sim 1200$  per spectral pixel. Since the planet signal is expected to be at least  $10^4$  times fainter than the starlight, it remains deeply buried in noise at this stage of the analysis.

The planetary scattered-light signature is present in each spectrum as a faint

Doppler-shifted copy of each of the star’s spectral lines. To build up this signal, we combine the velocity profiles of thousands of spectral lines using a least-squares deconvolution technique (LSD) that has become a standard tool for detecting and mapping stellar surface features<sup>5</sup>.

Our LSD procedure uses a list of the known wavelengths and strengths of  $\sim 2300$  spectral lines that are present over the observed wavelength domain in a star of  $\tau$  Boo’s temperature and composition. We determine, via  $\chi^2$  minimization, a “mean” line profile which, when convolved with the known line pattern, yields an optimally-weighted match to the strengths and shapes of the lines in the observed spectrum. This “deconvolved profile” is thus an average velocity profile that is representative of all the lines recorded in the spectrum, but with a vastly improved signal-to-noise ratio. Blends are automatically compensated for, so that LSD gives a flat continuum outside the stellar profile, free of the sidelobes that are produced by simpler shift-and-add or cross-correlation procedures. We first apply LSD to the spectra of  $\tau$  Boo, to establish the mean strength of its stellar absorption lines. A second application of LSD, this time to the template-subtracted spectra, extracts the mean velocity profile of the planetary signal averaged over all of those lines. The resulting template-subtracted velocity profiles, one for each spectrum, are displayed as a velocity-phase map in Fig.1.

The most prominent pattern visible in Fig. 1 is a “barber’s pole” pattern at low velocities inside  $\pm 28 \text{ km s}^{-1}$ . This pattern is the same when we split the data into several wavelength regions, suggesting a stellar origin rather than a problem in the template registration and subtraction. The ripples drift from the blue to the red wing of the profile in roughly half the orbital period of the planet. One possible explanation would be the presence of solar-sized starspot groups crossing the face of the star as it rotates synchronously with the orbit. The presence of large-scale inhomogeneities in the photospheric velocity field<sup>6</sup> could also give low-amplitude, rotationally-modulated distortion of the line profiles without producing significant

optical variability. A rotational modulation of the star’s chromospheric Ca II H & K emission has been detected with a period of 3.3 days<sup>7</sup>, essentially the same as the 3.312567-day orbital period of the planet. The barber’s-pole pattern thus provides useful independent confirmation that the star does indeed rotate synchronously with the planet’s orbit.

Outside the range  $\pm 28 \text{ km s}^{-1}$ , the residuals have the general appearance of random noise, but with some correlation in time due to nights with residual flat-fielding errors. The root-mean-square scatter indicates a signal-to-noise ratio of  $\sim 3.5 \times 10^4$  per spectral pixel relative to the original stellar continuum level. This noise level is 10% to 15% greater than photon noise estimates propagated through the data extraction and deconvolution. LSD has therefore realized a 30-fold increase in signal-to-noise ratio by combining the velocity profiles of the  $\sim 2300$  spectral lines. This should be just sufficient to detect the brightest expected planet signature in those of the 145 LSD velocity profiles taken at gibbous phases when the planet is Doppler-shifted well clear of the stellar profile.

To search for candidate planet signals, measure their strengths and assess their significance, and to quantify upper limits on planets at other inclinations, we must extract information from the LSD velocity profiles at all 145 orbital phases. We do this in an optimal way by using a matched filter to account for the expected changes in the planet’s Doppler shift and brightness with orbital phase.

We model the velocity profile of a planet signal as a moving Gaussian

$$G(v, \phi, K_p) = \frac{Wg(\phi, i)}{\sqrt{\pi}\Delta} \exp \left\{ - \left( \frac{v - K_p \sin \phi}{\Delta} \right)^2 \right\} .$$

The velocity width parameter  $\Delta$  is chosen to match the expected averaged width of the stellar lines reflected from the planet. Because the star rotates synchronously with the planet’s orbit, the planet sees the stellar spectrum without the rotational broadening that we see in the direct starlight<sup>8</sup>. We estimate the width parameters of the direct starlight and the reflected light to be 13.2 and 6.4  $\text{km s}^{-1}$  respectively,

from Gaussian fits to the deconvolved profiles of  $\tau$  Boo and the slowly rotating giant star HR 5694. The latter has an F7 III spectral type (temperature) and elemental abundances similar to  $\tau$  Boo<sup>7</sup>. The larger width and shallower depth of  $\tau$  Boo’s lines, due largely to the star’s axial rotation, yields<sup>9, 10, 11</sup> a projected equatorial rotation speed  $v \sin i = 14.8 \pm 0.3 \text{ km s}^{-1}$ , where  $i$  is the inclination of the spin axis to the line of sight.

The line strength parameter  $W$  is set to match that of  $\tau$  Boo. For  $g(\phi, i)$ , which modulates the planet’s brightness with orbital phase, we adopt an empirically-determined polynomial approximation to the phase function of Venus<sup>12</sup>. The orbital velocity amplitude is  $K_p = V_p \sin i$ , where  $V_p = 152 \text{ km s}^{-1}$ . Note that  $K_p$  and  $i$  are not independent parameters; we compute  $i$  for each value of  $K_p$ .

To compensate for the attenuating effect of a blurred planet signal being present in the template, we mimic the effect in constructing the matched filter  $M(v, \phi, K_p)$ . We do this by subtracting the flux-weighted average of the Gaussian planet signals on each night, emulating precisely the attenuation arising from the template construction and subtraction.

To allow for the possibility that the planet’s albedo is wavelength dependent, we subdivide our data into 6 independent wavelength ranges and measure the planet signal strength  $\epsilon(\lambda)$  in each data subset. Thus we construct template-subtracted LSD velocity profiles  $f(v, \phi, \lambda)$ , and their corresponding noise variances  $\sigma^2(v, \phi, \lambda)$ , for 6 independent subsets of the echelle orders at wavelengths  $\lambda$ . For any set of trial values of the parameters  $K_p$  and  $\epsilon(\lambda)$ , we quantify the “badness of fit” to the data by means of the standard  $\chi^2$  statistic

$$\chi^2 \equiv \sum_v \sum_\phi \sum_\lambda \left( \frac{f(v, \phi, \lambda) - \epsilon(\lambda)M(v, \phi, K_p)}{\sigma(v, \phi, \lambda)} \right)^2 .$$

Thus we scale the matched filter  $M(v, \phi, K_p)$  by factors  $\epsilon(\lambda)$  to fit LSD velocity profiles  $f(v, \phi, \lambda) \pm \sigma(v, \phi, \lambda)$ , which are like those shown in Fig. 1 but constructed from wavelength-restricted subsets of the data. The best fit minimizes  $\chi^2$ , yielding

the optimal estimates of  $K_p$  and  $\epsilon(\lambda)$ . The increase in  $\chi^2$  for nearby parameter values,  $\Delta\chi^2$ , is used to judge different models, their relative probabilities being proportional to  $\exp(-\Delta\chi^2/2)$ . To prevent spurious planet signatures arising from the “barber’s pole” pattern in the residual stellar profile, we exclude from the fitting procedure all pixels within  $31.5 \text{ km s}^{-1}$  of the centre of the stellar profile.

We verified that our procedure is capable of revealing faint planetary signals in the presence of realistic noise levels and patterns by adding a simulated planetary signal to the observed spectra, then repeating the template construction, subtraction and LSD analysis. The planet was simulated by the spectrum of HR 5694, Doppler shifted to the appropriate orbital velocities and scaled according to the phase function expected for a planet with a radius 1.4 times that of Jupiter and a grey albedo  $p = 0.55$  (Fig. 1).

In searching for candidate planetary signals in the WHT data, we begin by testing the null hypothesis that no planet is present, in comparison with the alternative hypothesis that a “grey” planet with wavelength-independent albedo is present at some value of  $K_p$ . We probe for evidence of a planet over the range  $40 \text{ km s}^{-1} < K_p < 152 \text{ km s}^{-1}$ , corresponding to inclinations  $15^\circ < i < 90^\circ$ . At lower velocities and inclinations the planet’s orbit velocity never emerges from the low-velocity region affected by the “barber pole” pattern. An inclination than  $i = 15^\circ$  would also require an implausibly high stellar equatorial rotation speed<sup>13</sup>.

Fig. 2 presents the relative probability map as a function of  $K_p$  and  $\epsilon$ , showing significant evidence for a planet at  $K_p = 74 \pm 3 \text{ km s}^{-1}$  and  $\epsilon = 7.5 \pm 3 \times 10^{-5}$ . The “grey-planet” hypothesis introduces 2 parameters,  $\epsilon$  and  $K_p$ . The improvement in the fit, reducing  $\chi^2$  by  $\Delta\chi^2 = 9.74$  with only 2 degrees of freedom, rejects the “no-planet” hypothesis with 97.8% confidence, based on a bootstrap analysis of the error distribution. Thus if no planet is present, the probability is about 2% that the noise in our data would produce a spurious signal this strong. When the synthetic planet signature at  $i = 60^\circ$  is injected into the data, its velocity amplitude and



strength are recovered correctly (Fig.2).

We examine next the hypothesis that the albedo depends on wavelength, by testing the “no-planet” hypothesis against a model with 7 additional parameters,  $K_p$ , and  $\epsilon(\lambda)$  for 6 wavelengths  $\lambda$ . Thus we split the data into six independent wavelength bands chosen so that the recorded flux is divided roughly equally among the six bands. By fitting independent values of  $\epsilon$  to different wavelength ranges we allow for the possibility that the planet’s albedo spectrum could contain broad absorption bands due to molecular species such as TiO overlying the main scattering layers. The greatest improvement in  $\chi^2$  occurs again at  $K_p = 74 \text{ km s}^{-1}$  (Fig. 3). With  $\Delta\chi^2 = 37.96$ , the “no-planet” hypothesis is again rejected, this time with 99.2% confidence for 7 degrees of freedom, an 0.8% probability of occurring by chance.

This result implies a significant departure from a wavelength-independent albedo spectrum. The signal is concentrated in the three wavelength bands from 456 nm to 524 nm, with the central 479 to 509 nm band contributing half of the signal. Averaging over these three bands alone, we obtain  $\epsilon = 1.9 \pm 0.4 \times 10^{-4}$ . No significant signal is present in the other bands redward and blueward of these three.

We conclude that there is strong evidence in our data for a planetary signal at  $K_p = 74 \text{ km s}^{-1}$ , which cannot easily be explained as a spurious detection caused by the photon statistics and locally correlated errors in our data.

The results obtained so far have relied on calculations of the planet’s orbital phase based on an orbit period  $P = 3.312567 \text{ d}$  and conjunction epoch  $T_0$  kindly communicated to us by G. Marcy. These parameters were derived from high-precision studies of the star’s velocity, and we are therefore justified in holding  $P$  and  $T_0$  fixed at their known values while searching for reflected-light signals over the feasible range of the unknown orbit velocities  $K_p$ . If the planet signal is strong enough, however, we should be able to measure  $P$  and  $T_0$  independently from our data, and those values should be consistent with the known values. Considering a small range around

Marcy’s values, our data yield  $P = 3.3128 \pm 0.0002$  days ( $1\sigma$  errors), consistent with Marcy’s more accurate period, and a conjunction phase  $\phi_0 = 0.007 \pm 0.003$ , consistent with Marcy’s  $0.000 \pm 0.002$ . Our measurement of  $K_p = 74 \pm 2$  km s<sup>-1</sup> is also insensitive to small changes in the period and epoch of the planet’s orbit.

We also considered different values for the velocity width  $\Delta$  of the absorption lines in the light scattered from the planet. The best fit was found for  $\Delta = 6 \pm 2$  km s<sup>-1</sup>. This is in good agreement with the 6.4 km s<sup>-1</sup> width of the lines in the spectrum of HR 5694, confirming that the planet sees the starlight without rotational broadening, and hence that the star rotates synchronously with the planet.

As an additional test, we use a periodogram analysis to estimate the probability that our planet signal could be an artifact of noise features that happen by chance to line up along the planet’s sinusoidal path in the velocity-phase diagram. For this test, we relax our knowledge of the planet’s orbital period  $P$ , and re-analyze the data for many different trial periods in the range  $3.25 < P < 3.35$  days. We estimate the “false-alarm” probability as the fraction of periods that yield a planet signal stronger than our candidate detection for some value of  $K_p$  in the feasible range. In order to keep the orbital phases close to 0.5 in the 1999 data for all periods considered, we set the time of zero phase to an epoch of conjunction just prior to 1999 May 5. The pattern of spurious peaks as a function of both  $K_p$  and  $P$  is then as shown in Fig. 4. The lower panel of this figure shows the minimum value of  $\chi^2$ , optimised over the range  $40 < K_p < 152$  km s<sup>-1</sup>, at each period. Of all the periods sampled, a small fraction yield spurious detections stronger than our planet signal, and close enough to their local maxima to pass the same local tests as our candidate signal.

We conclude from the periodogram test that the probability of encountering a spurious peak with  $K_p > 74$  km s<sup>-1</sup> is between 3 and 5 percent. This is our most pessimistic assessment of the probability that our detection is spurious. If other prior knowledge is taken into account – in particular, the restrictions imposed on the orbital inclination by the star’s synchronous rotation – the false-alarm probability

is reduced further still.

The best-fitting orbital velocity amplitude  $K_p = 74 \text{ km s}^{-1}$  yields an orbital inclination  $i = 29^\circ$  and implies a planet mass eight times that of Jupiter, twice the minimum value for an edge-on orbit. The low inclination is consistent with arguments for synchronous rotation, based on the star's equatorial rotation speed, rotation period, angular diameter and distance<sup>7, 10</sup>, plus the requirement that the star's rotational synchronisation timescale ( $1.2 \times 10^{11} \sin^8 i$  years) must then be shorter than its present age (less than  $\sim 3 \text{ Gyr}$ )<sup>14, 15</sup>.

At this low inclination, the fact that we are able to detect the planet at all suggests a large radius and/or reflectivity. Indeed, our planet-to-star flux ratio  $\epsilon = 1.9 \pm 0.4 \times 10^{-4}$ , averaged between 456 and 524 nm, appears to conflict with recent work<sup>13</sup> by Charbonneau et al., who establish an upper limit on the brightness of the  $\tau$  Boo planet  $\epsilon < 10^{-4}$  with 99.9% confidence for  $i \sim 30^\circ$  at similar wavelengths. We caution, however, that the value of  $\epsilon$  produced by our fitting method is sensitive to the Venus-like form we adopt for the phase function. A lower value of  $\epsilon$  and hence a smaller radius results if the true phase function is less strongly peaked at zero phase angle than the one used here. We also note that, while Charbonneau et al. estimate a  $\sim 20\%$  attenuation of planet signals due to their template-subtraction process, their tests recovering simulated planet signatures were incomplete because the template spectrum was fitted before rather than after adding the planet. We designed our matched-filter fitting function to mimic closely the effects of template attenuation. Our tests with recovery of synthetic planet signatures indicate that this was adequate to compensate for the effect. We conclude that differences in the treatment of the phase function and template attenuation effects are sufficient to reconcile the apparent conflict between our detection and the upper limit published by Charbonneau et al.

The radius we infer for  $\tau$  Boo's planet is 1.8 times that of Jupiter, assuming a Jupiter-like albedo  $p = 0.55$ , and using the Venus-like phase function. This is some-

what larger than the radii predicted by recent structural and evolutionary models<sup>16</sup>, which range from  $\sim 1.4 R_J$  at age 2 Gyr to  $\sim 1.1 R_J$  at 3 Gyr. If we use a Lambert-sphere model, as employed by Charbonneau et al., our measured radius decreases by 12% to  $1.6 R_J$ .

Our candidate detection of starlight scattered from the atmosphere of an extra-solar planet strengthens the case for the existence of the giant, close-orbiting planets whose presence has so far been inferred only indirectly from the reflex motions of their parent stars. The strength of the detection indicates that the  $\tau$  Boo planet is a gas giant, and suggests that its optical reflectivity may be appreciable only over a narrow range of blue-green wavelengths. Further observations will be needed to determine the form of the phase function, and so improve estimates of the radius and albedo. We envisage that it will be possible to infer the presence or absence of molecular species such as TiO, methane and water in the vapour phase, by carrying out more sensitive studies over suitably defined wavelength ranges. Finally, we note that the close-orbiting planets of both 51 Pegasi and the  $\nu$  Andromedae triple-planet system should be amenable to similar studies in the near future.

### *References*

- (1) Mayor, M. & Queloz, D. A Jupiter-mass companion to a solar-type star, *Nature*, **378**, 355–359, (1995)
- (2) Butler, R. P., Marcy, G. W., Williams, E., Hauser, H. & Shirts, P. Three new 51 Pegasi-type planets, *Astrophys. J.*, **474**, L115–L118, (1997)
- (3) Butler, R. P., Marcy, G. W., Vogt, S. S. & Apps, K. A planet with a 3.1 day period around a solar twin, *Publ. Astron. Soc. Pacific*, **110**, 1389–1393, (1998)
- (4) Fischer, D. A., Marcy, G. W., Butler, R. P., Vogt, S. S. & Apps, K. Planetary companions around two solar-type stars: HD 195019 and HD 217107, *Publ. Astron. Soc. Pacific*, **111**, 50–56, (1999)

- (5) Donati, J.-F., Semel, M., Carter, B., Rees, D. E. & Collier Cameron, A. Spectropolarimetric observations of active stars, *Mon. Not. R. Astron. Soc.*, **291**, 658–682, (1997)
- (6) Toner, C. G. & Gray, D. F. The starpatch on the G8 dwarf  $\xi$  Bootis A, *Astrophys. J.*, **334**, 1008–1020, (1988)
- (7) Baliunas, S. L., Henry, G. W., Donahue, R. A., Fekel, F. C. & Soon, W. H. Properties of sun-like stars with planets:  $\rho^1$  Cancri,  $\tau$  Bootis, and  $v$  Andromedae, *Astrophys. J.*, **474**, L119–L122, (1997)
- (8) Charbonneau, D., Jha, S. & Noyes, R. W. Spectral line distortions in the presence of a close-in planet, *Astrophys. J.*, **507**, L153–L156, (1998)
- (9) Gray, D. F. Observational evidence against differential rotation in F stars, *Astrophys. J.*, **258**, 201–208, (1982)
- (10) Fuhrmann, K., Pfeiffer, M. J. & Bernkopf, J. F- and G-type stars with planetary companions:  $v$  Andromedae,  $\rho^1$  Cancri,  $\tau$  Bootis, 16 Cygni and  $\rho$  Coronae Borealis, *Astron. Astrophys.*, **336**, 942–952, (1998)
- (11) Gonzalez, G. Spectroscopic analyses of the parent stars of extrasolar planetary system candidates, *Astron. Astrophys.*, **334**, 221–238, (1998)
- (12) Hilton, J. L. Physical ephemerides of the sun, moon, planets and satellites. in Seidelmann, P. K. (ed.), *Explanatory supplement to the Astronomical Almanac*, pages 383–419, Mill Valley, CA, 1992. University Science Books
- (13) Charbonneau, D., Noyes, R. W., Korzennik, S., Nisenson, P., Jha, S., Vogt, S. S. & Kibrick, R. I. An upper limit on the reflected light from the planet orbiting the star  $\tau$  Bootis, *Astrophys. J.*, **522**, L145–L149, (1999)

- (14) Marcy, G. W., Butler, R. P., Williams, E., Bildsten, L., Graham, J. R., Ghez, A. M. & Jernigan, J. G. The planet around 51 Pegasi, *Astrophys. J.*, **481**, 926–935, (1997)
- (15) Drake, S. A., Pravdo, S. H., Angelini, L. & Stern, R. A. Synchronization timescales for three solar-type stars that have Jupiter-mass companions in short-period orbits, *Astron. J.*, **115**, 2122–2124, (1998)
- (16) Guillot, T., Saumon, D., Burrows, A., Hubbard, W. B., Lunine, J. I., Marley, M. S. & Freedman, R. S. On the nature of the newly discovered extrasolar planets. in Cosmovici, C. V., Bowyer, S. & Wertheimer, D. (eds.), *IAU Colloquium 161: Astronomical and biochemical origins and the search for life in the Universe*, pages 343–350, Bologna, 1997. Editrice Compositori

**Acknowledgments:** This work is based on observations secured with the 4.2-m *William Herschel Telescope* at the Observatorio del Roque de los Muchachos on La Palma, and used *Starlink*-supported hardware and software. We thank the referees for helpful criticism.

Correspondence should be addressed to A.C.C. (e-mail [andrew.cameron@st-and.ac.uk](mailto:andrew.cameron@st-and.ac.uk)).

TABLE I

Journal of observations. The UTC mid-times and orbital phases are shown for the first and last groups of four spectra secured on each night of observation. The spectra spanned the optical wavelength range from 385 nm to 611 nm at a resolving power  $\lambda/\Delta\lambda = 49,000$ . The signal-to-noise ratio, typically  $\sim 600$  in each  $3 \text{ km s}^{-1}$  wide spectral pixel, was limited by photon statistics. The number of groups of four such consecutive spectra is given in the final column. The orbital phase  $\phi$  increases from 0 to 1 around the orbit, and is defined so that the planet is closest to the observer at phase 0. In the 1999 season we concentrated on the phase range between 0.4 and 0.6, where the planet is expected to be brightest. The orbital phases are computed from the epoch of inferior conjunction  $T_0$  at HJD 2451269.756 and orbital period  $P = 3.312567 \text{ d}$ , kindly communicated to us directly by G. Marcy.

UTC start	Phase	UTC End	Phase	Number of groups
1998 Apr 09 22:09:43	0.4254	1998 Apr 10 05:37:05	0.5192	25
1998 Apr 10 22:04:40	0.7262	1998 Apr 11 06:20:54	0.8303	29
1998 Apr 11 22:09:28	0.0291	1998 Apr 12 05:58:44	0.1275	21
1998 Apr 13 23:02:54	0.6441	1998 Apr 14 06:08:23	0.7332	9
1999 Apr 02 22:06:45	0.4931	1999 Apr 03 06:08:47	0.5941	15
1999 Apr 25 21:43:17	0.4411	1999 Apr 26 05:31:59	0.5393	10
1999 May 05 21:56:59	0.4628	1999 May 06 04:51:57	0.5497	15
1999 May 25 20:59:45	0.4884	1999 May 26 03:56:18	0.5757	11
1999 May 28 21:06:19	0.3954	1999 May 29 02:40:44	0.4655	10

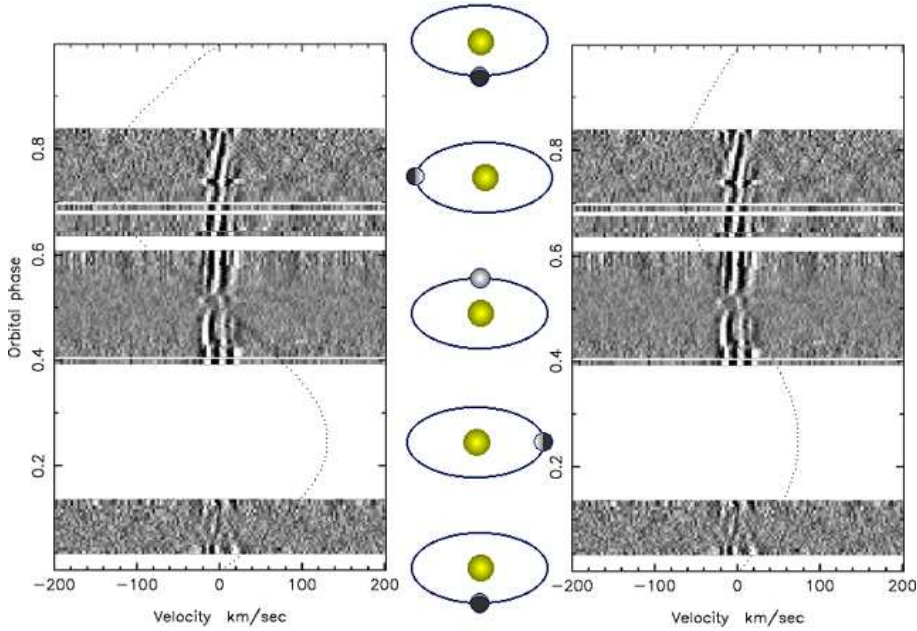


FIGURE 1

Greyscale plots showing the 145 residual velocity profiles that arise from subtracting the stellar template model and averaging the profiles of  $\sim 2300$  spectral lines in each of the 145 spectra. The velocity scale is in the reference frame of the star, and time increases upward. The orientation of the system at each orbital phase is sketched at centre. The greyscale runs from black at  $-10^{-4}$  to white at  $+10^{-4}$  times the mean stellar continuum flux. The dotted paths indicate the velocity curve of a planet orbiting with an orbital inclination of  $29^\circ$  (left-hand panel) and  $60^\circ$  (right-hand panel). The right-hand panel shows the effect of adding the simulated spectrum of a planet with 1.4 Jupiter radii and a geometric albedo of 0.55 to the original spectra. The signature of this simulated planet appears as a dark linear feature crossing from  $+80 \text{ km s}^{-1}$  at phase 0.4 to  $-80 \text{ km s}^{-1}$  at phase 0.6. The planetary signature detected in the data is much weaker, because of the low inclination, but would follow the velocity curve shown in the left-hand panel. The “barber’s pole” pattern of travelling ripples lies wholly within the residual stellar profile and has a characteristic amplitude 2 to  $4 \times 10^{-4}$  of the mean stellar continuum level. Its form remains invariant in profiles deconvolved from independent subsets of the data at different wavelengths. All data between phases 0.64 and 0.83 were obtained in a 5-night interval during the 1998 season. The ripple pattern appears both stronger and more coherent here than in the 1999 dataset, with 5 nights spread over 2 months selecting orbital phases near 0.5



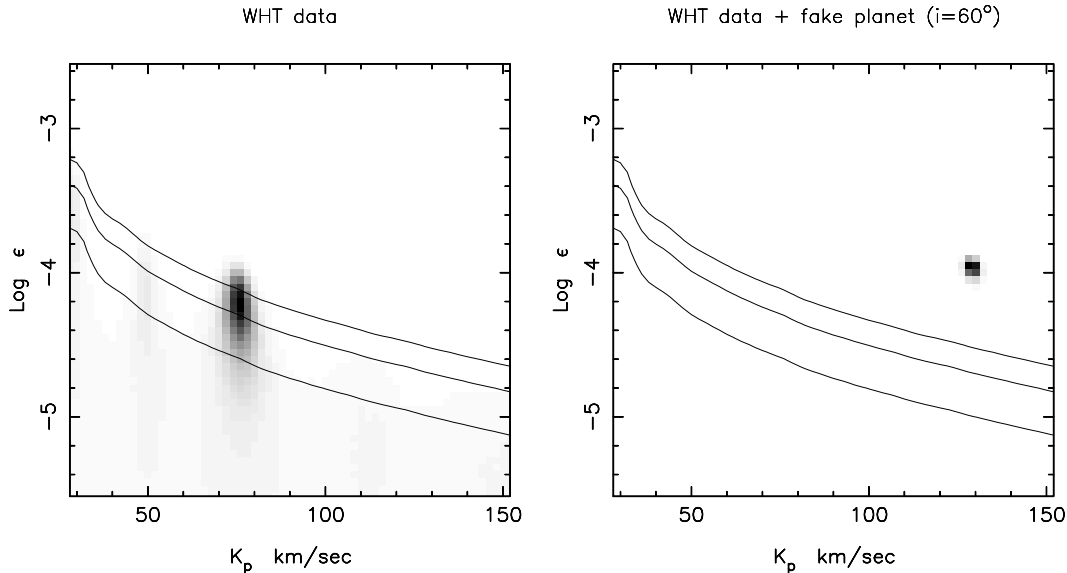


FIGURE 2

The improvement in the fit to the data is shown for the assumption of a planet with a wavelength-independent (grey) albedo. The two panels present identical analyses of the residual velocity profiles shown in the corresponding panels of Fig. 1, representing the WHT data alone (left) and the WHT data after adding a simulated planet signal for  $i = 60^\circ$  (right). For each possible value of the unknown planet-to-star brightness ratio  $\epsilon$ , and of the planet’s projected orbit velocity  $K_p$ , darker shades denote progressively better fits to the data. The probability relative to the best-fit model increases from 0 for white to 1 for black. In the right panel, the fake planet’s parameters  $K_p = 132 \text{ km s}^{-1}$  and  $\epsilon = 1.07 \times 10^{-4}$  are correctly recovered. In the left panel, the best fit to the WHT data occurs for  $K_p = 74 \text{ km s}^{-1}$  and  $\epsilon = 7.5 \times 10^{-5}$ . The “grey-planet” model significantly improves the fit (darker shading) relative to the “no-planet” model ( $\epsilon = 0$ ); the improvement in  $\chi^2$  after optimizing  $\epsilon$  and  $K_p$  is  $\Delta\chi^2 = 9.74$ . If no planet were present, the probability of such an improvement occurring by chance should have a  $\chi^2$  distribution with 2 degrees of freedom. The actual distribution, derived for the noise and systematic error in our data via a bootstrap error analysis, has a slightly longer tail, so that  $\Delta\chi^2 = 9.74$  rejects the “no-planet” hypothesis with 97.8% confidence. If no planet is present, the best-fit model should lie below the 68.3%, 95.4%, and 99.7% bootstrap confidence limits shown as solid curves. These limits decrease with  $K_p$  because for larger  $K_p$  the planet lines move more rapidly across the stellar profile and into the region covered by the data between phases 0.4 and 0.6. The light grey shading below the confidence limits is consistent with noise, and planets are strongly excluded in the white zones above the highest confidence limit.

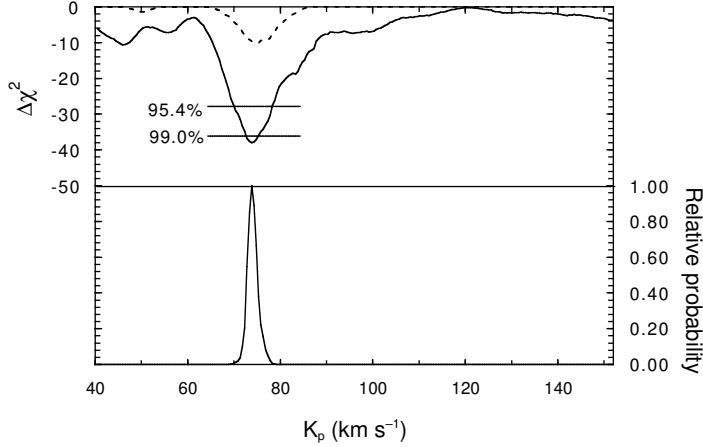


FIGURE 3

The evidence for a planet in the WHT data is assessed as a function of the planet's orbit velocity  $K_p$ . The top panel gives  $\Delta\chi^2$ , the reduction in the  $\chi^2$  of the fit relative to the assumption that no planet is present, for the 2-parameter model in which the planet is assumed to have constant (grey) albedo (dashed curve), and for the 7-parameter model with the planet's albedo varying with wavelength (solid curve). The horizontal lines give for two values of  $\Delta\chi^2$  the corresponding probabilities that the improvement in  $\chi^2$  is too large to be attributed to noise. The 2-parameter constant albedo model gives a significant (97.8%) improvement at  $K_p = 74 \text{ km s}^{-1}$ , and the wavelength-varying albedo model with 7 fitted parameters raises this probability to 99.2%. The lower panel shows the probability of the 7-parameter model as a function of  $K_p$ , scaled to 1 for the best-fit model  $K_p = 74 \pm 2 \text{ km s}^{-1}$ .

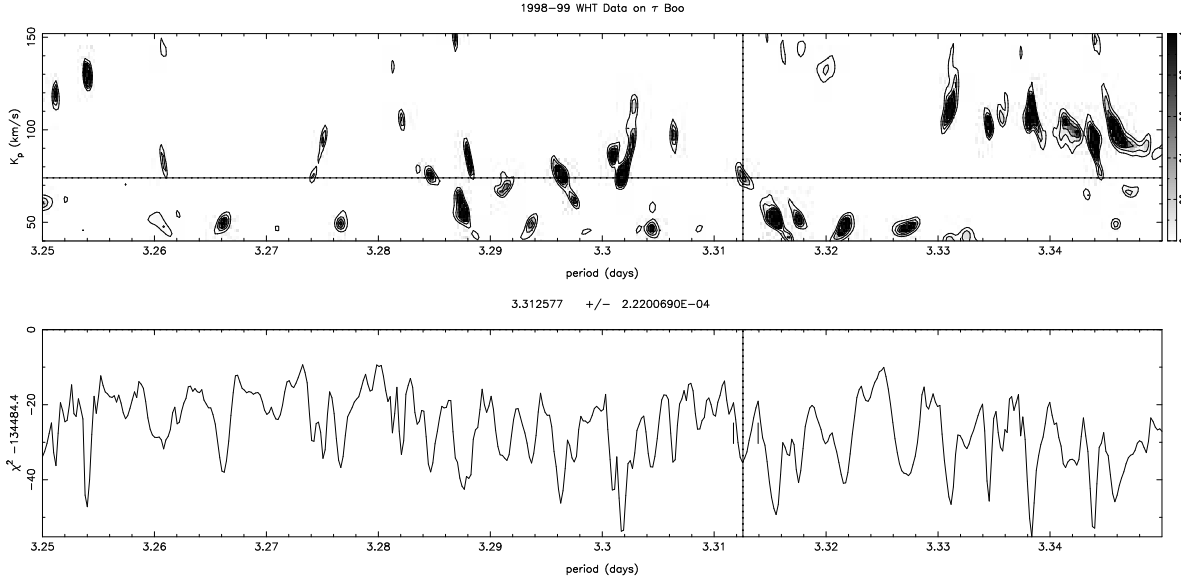


FIGURE 4

This periodogram analysis searches for evidence of reflected light from the  $\tau$  Boo planet over a range of trial values of the orbit velocity  $K_p$  and orbit period  $P$ . For each value of  $K_p$  and  $P$ , the 6 values  $\epsilon(\lambda)$  are optimized to fit 6 independent wavelength subsets of the echelle data. The lower panel shows the best  $\chi^2$  found for  $K_p$  between 40 and 152 km s $^{-1}$  at each trial period  $P$ . In the upper panel, the greyscale indicates for each value of  $K_p$  and  $P$  the relative probability of the best-fit model, with white to black representing increasing relative probability. The vertical line marks the accurate value of  $P$ , from G. Marcy’s analysis of the star’s Doppler signal. Our detection is the probability peak occurring at the correct period near  $K_p = 74$  km s $^{-1}$ , as marked by the intersection between the vertical and horizontal lines. The contours give  $1\sigma$ ,  $2\sigma$ , and  $3\sigma$  confidence regions for this peak, based on  $\Delta\chi^2$  for 2 degrees of freedom. A number of other peaks, some giving even better fits to the data than our detection, are seen at different values of  $P$  and  $K_p$ . These peaks arise mainly from noise in the data. We infer from the number of such peaks that there is a 3 to 5% probability that our detection is a spurious noise peak that happens by chance to coincide with the known period. Note that some periodogram features appear twice, shifted horizontally by 0.03 days. These correspond to pairs of periods that differ by 1 orbital cycle per year, due to the 1 year gap that separates our 1998 and 1999 observations.